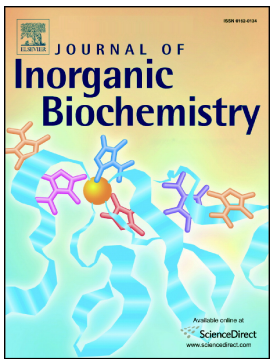

Dual functions of iridium(III) 2-phenylpyridine complexes: Metastasis inhibition and lysosomal damage

Xicheng Liu, Shujiao Chen, Xingxing Ge, Ying Zhang, Yaoqi Xie, Yingying Hao, Daiqun Wu, Jinmin Zhao, Xiang-Ai Yuan, Laijin Tian, Zhe Liu

PII: S0162-0134(19)30559-8

DOI: https://doi.org/10.1016/j.jinorgbio.2019.110983

Reference: JIB 110983

To appear in: *Journal of Inorganic Biochemistry*

Received date: 23 August 2019

Revised date: 11 December 2019

Accepted date: 26 December 2019

Please cite this article as: X. Liu, S. Chen, X. Ge, et al., Dual functions of iridium(III) 2-phenylpyridine complexes: Metastasis inhibition and lysosomal damage, *Journal of Inorganic Biochemistry* (2018), https://doi.org/10.1016/j.jinorgbio.2019.110983

Dual functions of Iridium(III) 2-phenylpyridine complexes: metastasis inhibition and lysosomal damage

Xicheng Liu[+]*, Shujiao Chen[+], Xingxing Ge, Ying Zhang, Yaoqi Xie, Yingying Hao, Daiqun Wu, Jinmin Zhao, Xiang-Ai Yuan, Laijin Tian, Zhe Liu*

Institute of Anticancer Agents Development and Theranostic Application, The Key Laboratory of Life-Organic Analysis and Key Laboratory of Pharmaceutical Intermediates and Analysis of Natural Medicine, School of Chemistry and Chemical Engineering, Qufu Normal University, Qufu 273165, China.

*Corresponding authors, Email: chemlxc@163.com (X. Liu); liuzheqd@163.com (Z. Liu)

[+] *X. Liu and S. Chen have equivalent contributions.*

Abstract: Six *N*-phenylcarbazole/triphenylamine-appended half-sandwich iridium(III) 2-phenylpyridine complexes ([(η^5-Cp*)Ir(C^N)Cl]) were prepared and characterized. Compared with cisplatin, these complexes exhibited potential antitumor activity against A549 and HeLa tumor cells, with IC_{50} values (half-maximum inhibitory concentration) that changed from 2.8 ± 0.8 μM to 39.5 ± 2.7 μM, and could block the migration of tumor cells. These complexes also effectively bound to protein (binding constant: ~10^4 M^{-1}) and were transported through serum proteins, catalyzed the oxidation of coenzyme nicotinamide-adenine dinucleotide. Additionally, laser confocal microscopy and flow cytometry confirmed that these complexes possessed a non-energy-dependent cellular uptake mechanism, effectively accumulated in lysosomes (Pearson colocalization coefficient: ~0.74), damaged the integrity of acidic lysosomes, led to a change in the mitochondrial membrane potential, disrupted the cell cycle (G_0/G_1 phase), and eventually induced apoptosis. Above all, these complexes are potential antitumor agents with dual functions: metastasis inhibition and lysosomal damage.

Keywords: Iridium(III) complexes; Antitumor; Metastasis inhibition; Lysosomal damage

1. Introduction

Lysosomes, which are acidic intracellular organelles (pH: 4.5–5.5), are related to many cellular processes, including apoptosis, cell migration, metabolism, plasma membrane repair and the extracellular release of active enzymes [1,2]. In tumor cells, lysosomes are more numerous,

less stable and show better cathepsin activity than that in normal cells, which can degrade almost all kinds of biomacromolecules through the actions of more than 50 acid hydrolytic enzymes [3]. Interestingly, studies indicated that weakly basic drugs could effectively accumulate in lysosomes, induce lysosomal swelling and rupture, and eventually, lead to lysosomal membrane permeabilization (LMP) [4]. In general, LMP causes the release of cathepsins and other hydrolases from the lysosomal lumen to the cytosol, thus inducing apoptosis or necrotic cell death [5]. Above all, lysosomes are attractive targets for the selective killing of tumor cells [6-7]. Agents that can interact with lysosomes, show promise for the development of novel and potent antitumor drugs.

Due to their unique antitumor mechanisms, including the inhibition of multiple protein activities and involvement in cellular redox reactions, iridium(III) (Ir^{III}) complexes have recently emerged as promising alternatives to platinum-based metallodrugs (cisplatin, carboplatin and oxaliplatin *etc.*) [8-11]. Among these, half-sandwich Ir^{III} complexes have attracted particular attention because of their favorable stability and antitumor activity [12-14]. The general formula for half-sandwich Ir^{III} complexes can be expressed as [(η^5-Cp*)Ir(L^L)Cl], where Cp* represents the electron-rich pentamethylcyclopentadienyl or its derivatives (*e.g.*, phenyl, biphenyl), L^L is various chelating ligands (*e.g.*, N^N, C^N, N^O and C^O), and Cl is the leaving group. Due to the easy modification of L^L ligands, a large number of weakly basic groups containing free electron pairs, *e.g.*, morpholine [15], benzimidazole [16, 17], rhodamine [18], *β*-carboline [19], and imine-*N*-heterocyclic carbene [7], have been introduced into Ir^{III} complexes and used as lysosome-targeted and real-time tracking drugs, achieving ideal results.

Triphenylamine (TPA), *N*-phenylcarbazole (PhCz) and their derivatives, which are typical hole-transporting and light-emitting materials, are widely used in organic light-emitting diodes (OLEDs) [20], perovskite solar cells (PSCs) [21-23], electrostatic copying devices (OFETs) [24] and electrostatic photocopying [25], *etc*. Additionally, these materials show promise for applications in the biological probe and drug-targeting fields due to their favorable luminescent properties, *e.g.*, low excitation energy, high fluorescence quantum yield, suitable energy level, favorable light and thermal stability. TPA-based spirobifluorene (SPF-TSA) enabled the fluorescent imaging of both probe and mercury ions in cells by two-photon microscopy and possessed excellent indicator properties within the acidic pH range [26, 27]. TPA-modified cyclometalated Ir^{III} phenanthroline complexes could effectively induce the production of singlet

oxygen ($^1O_2$) after 730 nm laser irradiation and acted as an effective phototherapy drug against HeLa cells [28]. In view of the favorable application prospects of triphenylamine in biological probes and anticancer complexes, PhCz/TPA-modified half-sandwich Ir^{III} phenylpyridine complexes were synthesized and characterized (Figure 1). The antitumor activity of these complexes against A549 (human lung cancer cells) and HeLa (human cervical cancer cells) cells was assessed by MTT (3-(4,5-dimethylthiazol-2-yl)-2,5-diphenyl tetrazolium bromide) assay, and the antitumor mechanism was studied through flow cytometry. Due to the favorable target fluorescent properties, laser confocal technology was used to investigate the cellular uptake and target sites in cells. Above all, PhCz/TPA-appended Ir^{III} complexes are potential antitumor agents for further evaluation.

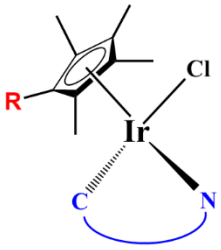

Complex	C^N	R
1	L1	CH_3
2	L1	C_6H_5
3	L2	CH_3
4	L2	C_6H_5
5	L3	CH_3
6	L3	C_6H_5

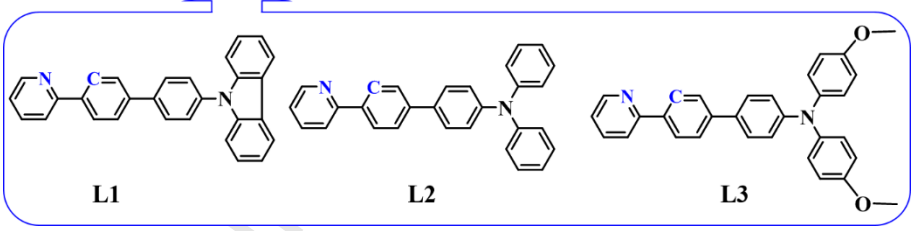

Figure 1. Structures of C^N chelating ligands (**L1**-**L3**) and target complexes (**1**-**6**).

2. Results and discussion

The synthetic strategy for PhCz/TPA-modified phenylpyridine (C^N) chelating ligands (**L1**-**L3**) and target Ir^{III} complexes (**1**-**6**) is described in Scheme 1. Among these, **L1**-**L3** were synthesized by brominated PhCz/TPA (**M1**) and 4-(2-pyridyl)phenylboronic acid (**M2**) with good yields (>80%) through the classical Suzuki reaction (palladium tetraphenylphosphine [$Pd(PPh_3)_4$] as catalyst, anhydrous potassium carbonate (K_2CO_3) as acid binding agent) [29]. Target Ir^{III} complexes were obtained by the reaction of iridium dimers (**Dimer 1** and **2**) and C^N chelating ligands (**L1**-**L3**), and sodium acetate (NaOAc) used as the acid extractor [30]. Structures and compositions of chelating ligands and target complexes were confirmed by ^1H NMR, elemental

analyses, mass spectroscopy (MS) analyses, and ^{13}C NMR. Chloroform-d ($CDCl_3$, 7.26 ppm) was used as a solvent for testing the ^{1}H NMR spectrum of Ir^{III} complexes. Hydrogen atoms of the five methyl groups on cyclopentadienyl (Cp) were shown in the range of 1.59 to 1.90 ppm in the ^{1}H NMR spectrum, the methoxyl of TPA groups was present at 3.81 ppm, and hydrogen atoms on the benzene and pyridine were in the range of 6.5 to 9.0 ppm. Ir^{III} complexes used multiple solvents such as dichloromethane (5.30 ppm) and acetic acid (2.10 ppm) in the synthesis and purification processes, which showed certain amounts of residue in the ^{1}H NMR spectrum. The MS data agreed well with the results of the theoretical calculation (chloride ion loss).

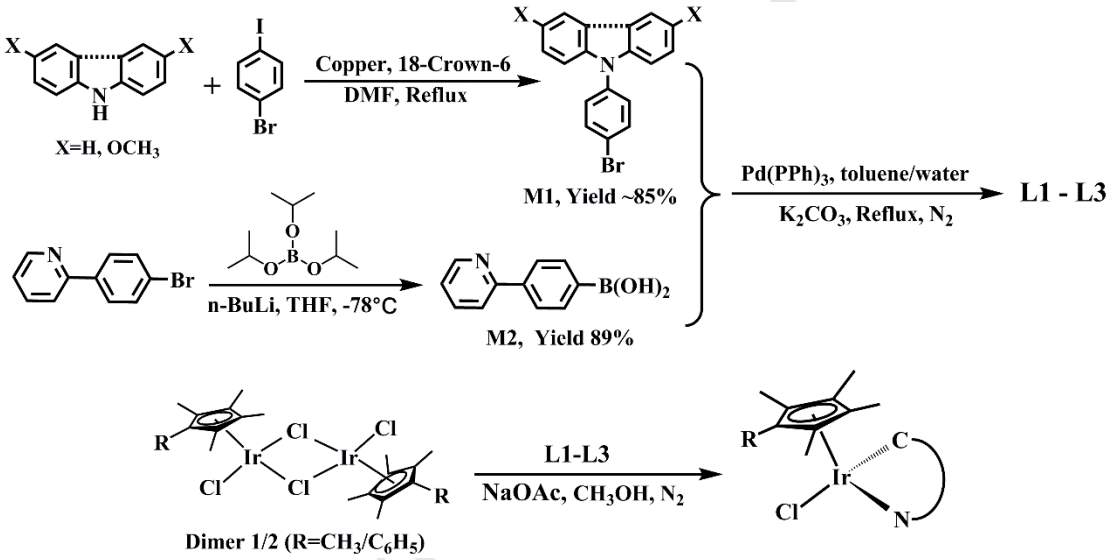

Scheme 1. Design strategy of chelating ligands and target Ir^{III} complexes.

Single crystals suitable for X-ray diffraction analysis were obtained by the slow diffusion of *n*-hexane into a saturated tetrahydrofuran solution of [(η^5-C_5Me_5)Ir(**L2**)Cl] (complex **3**). The X-ray crystal structure is illustrated in Figure 2, and the crystallographic data are listed in Tables S1 and S2. Complex **3** shows the expected half-sandwich "three-leg piano-stool" geometry, and the terminal TPA group exhibits a "propeller" shape with dihedral angles of 65.71, 74.41 and 75.29°. Additionally, the angle between **P1** (benzene ring of phenylpyridine) and **P2** (benzene ring of TPA) is 34.87°. The smaller angle ensures the good coplanar property of the chelating ligand and further improves its electron donor ability. The distance from the central iridium ion to the cyclopentadiene ring is 1.832 Å, and the bond distances of Ir-N1, Ir-C7 and Ir-C1l are 2.095, 2.028 and 2.411 Å, respectively. The longer bond lengths correspond to the notion that the Ir-Cl bond is the active center for half-sandwich Ir^{III} complexes [12].

It is worth noting that the stability of complexes in solution is closely related to their biological activity [12]. Therefore, the stability of complexes **1-6** in a mixture of 20% MeOH/80% phosphate buffered saline (PBS: pH ≈ 7.2, PBS is prepared from H_2O) were evaluated by ultraviolet-visible spectra at 25 ℃. As shown in Figure S1, complexes did not show significant changes within 8 h, which indicating that Ir^{III} complexes are fairly stable and provide conditions for subsequent biological assays.

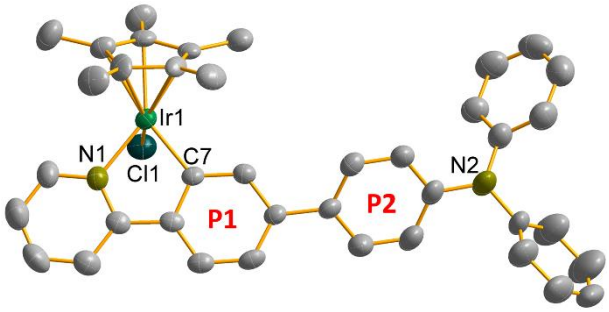

Figure 2. Molecular structure of complex **3** (Hydrogen atoms have been omitted for clarity).

2.1. Cytotoxicity and antimetastatic assay

The antitumor activity of PhCz/TPA-appended half-sandwich Ir^{III} phenylpyridine (PhPy) complexes against A549 (human lung cancer) and HeLa (human cervical cancer) cells was ascertained by the MTT assay after 24 h of treatment. The IC_{50} values (concentration when 50% cell growth was inhibited) of complexes **1-6**, cisplatin, and complexes **7** and **8** (Scheme S1, half-sandwich Ir^{III} 2-phenylpyridine complexes) are listed in Table 1. These complexes showed better antitumor activity, the best of which (complex **1**) was nearly eight times that of cisplatin (widely used in the clinic) under the same conditions**.** Additionally, compared with the iridium dimers (**Dimer 1** and **2**), chelating ligands (**L1-L3**) and complexes **7** and **8** , target complexes exhibited better antitumor activity (Table S3), which confirms that the introduction of a PhCz/TPA unit is beneficial for improving the antitumor activity of these complexes.

Table 1. IC_{50} values of complexes and cisplatin against A549, HeLa and BEAS-2B cells.

Complex	IC_{50} (μM)		
	A549	HeLa	BEAS-2B
[(η^5-C_5Me_5)Ir(**L1**)Cl] (**1**)	2.8±0.8	1.6±0.2	1.9±0.1
[(η^5-$C_5Me_4C_6H_5$)Ir(**L1**)Cl] (**2**)	23.0±0.7	7.3±1.6	7.0±1.5
[(η^5-C_5Me_5)Ir(**L2**)Cl] (**3**)	7.4±0.1	2.5±0.1	1.6±0.5

[(η^5-$C_5Me_4C_6H_5$)Ir(**L2**)Cl] (**4**)	39.5±2.7	40.6±2.8	45.7±1.4
[(η^5-C_5Me_5)Ir(**L3**)Cl] (**5**)	3.5±0.1	1.3±0.1	1.7±0.2
[(η^5-$C_5Me_4C_6H_5$)Ir(**L3**)Cl] (**6**)	13.0±0.5	8.6±0.6	11.8±2.4
[(η^5-C_5Me_5)Ir(PhPy)Cl] (**7**)	27.6±0.6	35.6±1.6	17.1±4.9
[(η^5-$C_5Me_4C_6H_5$)Ir(PhPy)Cl] (**8**)	8.5±1.4	11.0±0.1	11.9±0.7
Cisplatin	21.3±1.7	7.5±0.2	38.4±2.8

Footnotes: The type of analysis is sample repeat; Exposure time is 24 h; A549 and HeLa cells are cancer cells, and BEAS-2B: non-malignant human bronchus epithelial cell line; Each is repeated at least three times.

Additionally, complexes containing a pentamethylcyclopentadienyl (η^5-C_5Me_5) ring (complexes **1**, **3** and **5**) showed better antitumor activity than that of the corresponding phenyl analogues (η^5-$C_5Me_4C_6H_5$, complexes **2**, **4** and **6**). To understand these results, quantum chemical computation was used for assessment after comprehensively considering the crystal structure of complex **3**. As shown in Figure S2, the natural population analysis (NPA) data for the central iridium atom and the leaving group (Cl) were analyzed by density functional theory (DFT) calculation at the B3LYP/6-31G(d, p) (C, H, N, Cl)/SDD (Ir) level [31, 32]. The NPA charge population for Cl was almost the same, with values of -0.373 and -0.374; however, that of Ir was 0.078 and 0.147 in complexes **3** and **4**, respectively. Obviously, the lower the charge of the central iridium ion for complex **3**, the more vulnerable it is to loss of the chloride ion, and the better the anticancer activity [12]. Inductively coupled plasma mass spectrometry (ICP-MS) indicated that the values of *logP* (partition coefficient in oil/water) were -0.19 and -0.75 for complexes **3** and **4**, respectively. The cumulative amount (equivalent concentration) of these complexes in A549 cells after 12 h incubation was measured. The cell accumulation of complexes **3** and **4** were 85.6 and 39.8 (ppb/10^6 cells), respectively. All these indicate that improved lipid solubility is beneficial for enhancing the antitumor activity of these complexes (**1, 3** and **5** > **7**); however, "going too far is as bad as not going far enough", and overlarge lipid solubility was unfavorable to the improvement of antitumor activity (**1>2**; **3>4**; **5>6; 2, 4** and **6＜8**), which provides a basis for the design of these complexes. The cytotoxicity of target complexes was further evaluated toward human lung epithelial cells (BEAS-2B, **Table 2**). However, the results were unsatisfactory, and there was no

significant selectivity between tumor cells and normal cells. Hence, more structural modification is necessary in future work to decrease the cytotoxic action against normal cells without loss of potential antitumor activity.

In general, tumor cell metastasis refers to the process of continuing to grow from the primary site through lymphatic vessels, blood vessels or body cavities to other normal sites; therefore, metastasis inhibition is an effective means of tumor treatment. Wound healing assays are an effective approach to assess the antimetastatic capacity of target complexes [33]. As shown in Figure 3, A549 cells treated with or without complexes **1** and **2** ($0.25 \times IC_{50}$) for 24 h, and the middle area between two blue lines ("Wound") is clear of tumor cells. In the absence of target complexes (Control), the wound closure ratio ($WCR = (R_0-R_1)/R_0 \times 100\%$) significantly improved after 24 h (WCR: 25.00%), which confirmed the migration characteristics of tumor cells. However, after the addition of complexes in this wound area, especially for **1**, the WCR value (9.47%) was relatively inhibited. This conclusion is consistent with the results of the MTT assay (**1** showed better antitumor activity than **2**) and also confirms that these complexes have a potential effect on the migration of cancer cells, which is helpful for tumor therapy.

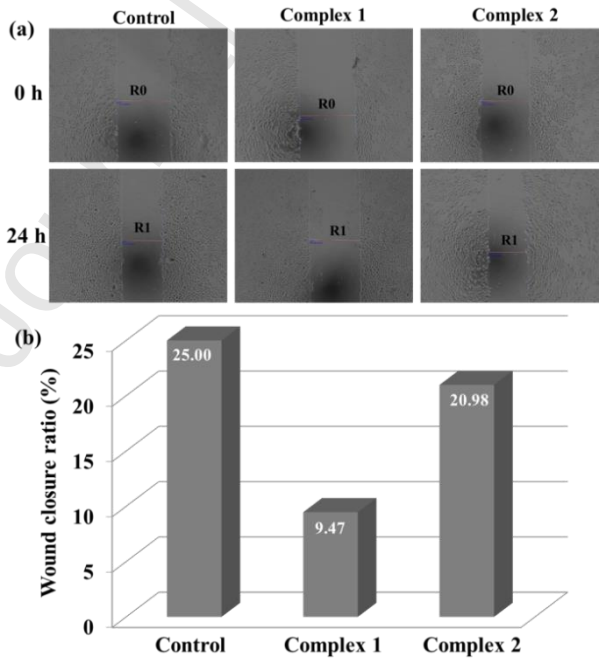

Figure 3. Wound healing assay of A549 cells treated with or without complexes **1** and **2** ($0.25 \times IC_{50}$) for 24 h. (a) Typical images were taken at 0 and 24 h. The widths of wounds are indicated with red lines. (b) Quantification of wound closure ratio.

2.2. Protein Binding assay

Serum albumin (SA), which is plentiful in blood plasma, plays an indispensable role in drug transport and supersession. Interactions between drugs and SA are helpful for understanding the intracellular situation [34]. Due to its structural homology with human serum albumin (HSA), bovine serum albumin (BSA) offers a cost-effective model for protein binding; therefore, it was utilized to study the binding characteristics with target complexes in this study.

As shown in Figures 4a and S3, the UV-vis absorption of BSA (10.0 μM) with or without target Ir^{III} complexes in Tris-HCl buffered solution (trishydroxymethylaminomethane- hydrochloric acid, pH = 7.2) possesses two absorption peaks. With the increase in complexes (0-10.0 μM), the maximum absorption at 228 nm (the absorption of BSA) decreased, which indicated that these complexes can act on BSA and induce α-helical interference. Meanwhile, a significant red shift (~6 nm) was found at 228 nm due to the influence of water (polar solvent). The absorption at 278 nm increased with the addition of complexes, which is related to the presence of three major amino acid residues (tryptophan, tyrosine and phenylalanine) in BSA. Therefore, simultaneous fluorescence spectra were utilized to ascertain the detailed changes of the microenvironment around BSA under similar conditions. In this study, tyrosine and tryptophan residues of BSA were detected through the wavelength intervals of $\Delta\lambda$ = 15 nm and 60 nm by synchronous fluorescence, respectively [35]. The weaker intensity of fluorescence at 291 nm and 285 nm ($\Delta\lambda$ = 15 nm and 60 nm, respectively) for complexes **1**-**6** is shown in Figures 4c, 4d, S4 and S5. Interestingly, a minor blue shift (~3 nm) is found at $\Delta\lambda$ = 60 nm; however, almost no change occurs at the wavelength of $\Delta\lambda$ = 15 nm, which indicates that target complexes can affect the conformation of the tryptophan microregion in BSA, in addition to tyrosine [36].

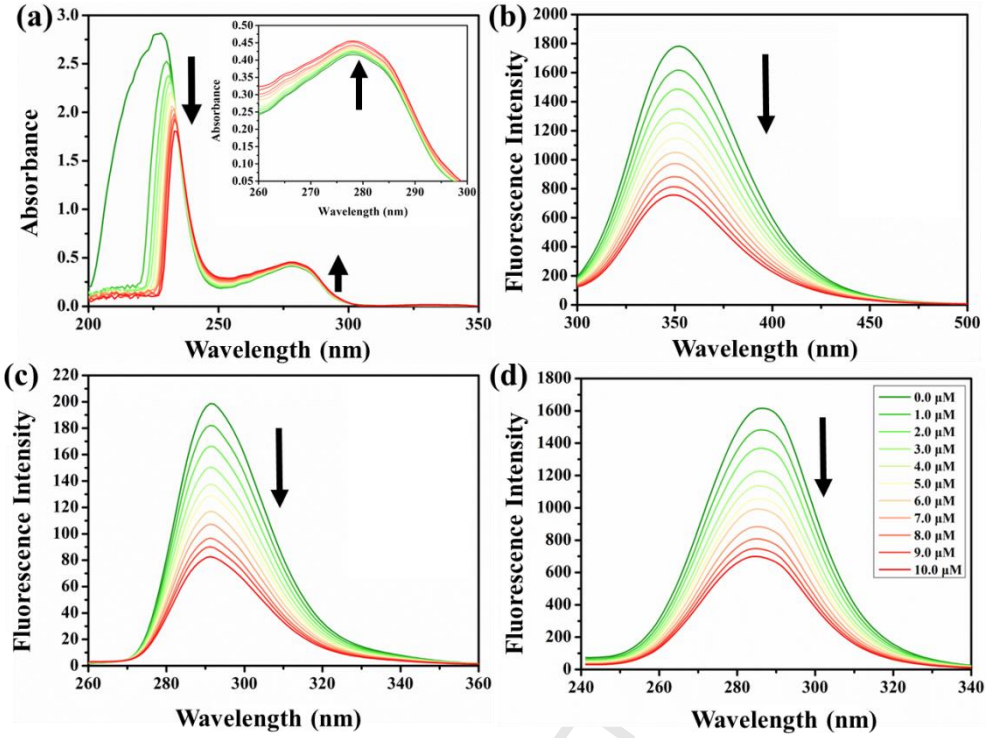

Figure 4. (a) UV-vis spectrum of BSA (10.0 μM, 50.0 mM Tris-HCl, 50.0 mM NaCl, pH = 7.2) reacted with complex **1** (0-10.0 μM). Inset: Wavelengths from 260 to 300 nm; (b) fluorescence spectra of BSA (10.0 μM; λ_{ex} = 280 nm; λ_{em} = 350 nm) in the absence and presence of complex **1** (0.0-10.0 μM); synchronous spectra of BSA (10.0 μM) with the addition of complex **1** (0.0-10.0 μM) with wavelength differences of $\Delta\lambda$ = 15 nm (c) and $\Delta\lambda$ = 60 nm (d). The arrow shows the changes in intensity with increased complexes.

The interaction between target complexes and BSA was further confirmed by the fluorescence quenching phenomenon of BSA [37]. As shown in Figures 4b and S6, with the addition of target complexes, the fluorescence intensity of BSA rapidly quenched. Generally, the quenching mechanism can be ascertained by the classical *Stern-Volmer* equation (***Equation* 1**) [38]:

$$F_0/F = 1 + K_{sv}[Q] = 1 + K_q\tau_0[Q] \qquad (1)$$

where K_q and K_{sv} represent the *Stern-Volmer* quenching rate constant and quenching constant (obtained by the slope of the *Stern-Volmer* equation, Figure S7), F_0 and F are the steady-state fluorescence intensities without or with target complex, τ_0 is the average life span of fluorophore without complex (10^{-8} s) and $[Q]$ is the concentration of complex. As shown in Table 2, the linear fitting *Stern−Volmer* plots represent a single quenching mechanism. The values of K_q (changed

from 0.76 × 10^{13} to 1.45 × 10^{13} $M^{-1}s^{-1}$) are far greater than the limit of the dynamic quenching mechanism (2.0 × 10^{12} $M^{-1}s^{-1}$), which indicates that these Ir^{III} complexes bind to BSA followed by the static quenching mechanism [39]. Additionally, the binding constant (K_b) and the numbers of binding sites (n) can be obtained through the *Scatchard* equation [40] (***Equation* 2**):

$$log[(F_0 - F)/F] = log\, K_b + n\, log[Q] \qquad (2)$$

The binding constant K_b reflects the degree of interaction between target complexes and BSA, and the values of n are the numbers of binding sites. As shown in Figure S8, K_b and n are the data after the linear fitting of $log((F_0 - F)/F)$ *vs* $log[Q]$. As shown in Table 2, the values of n are almost the same (~1) for all complexes, which is consistent with the results showing that the binding between BSA and Ir^{III} complexes can affect the conformation of the tryptophan microregion. In addition, the binding constants (K_b) of complexes **1**, **3** and **5** are a little bigger than those of homologous phenyl-modified complexes (**2**, **4** and **6)**, respectively, which is also consistent with the results of the cytotoxicity test. Above all, BSA may be an excellent carrier for the delivery of these complexes in *vivo*.

Table 2. The values of K_{sv}, K_b, K_q and n for complexes **1-6** at 298 K.

Complex	K_{sv} (10^5 M^{-1})	K_q (10^{13} M^{-1} s^{-1})	K_b (10^4 M^{-1})	n
1	1.20±0.20	1.20	10.16	1.05
2	1.11±0.21	1.11	7.99	1.08
3	1.45±0.15	1.45	9.42	1.13
4	0.76±0.10	0.76	5.68	1.10
5	1.55±0.19	1.55	9.44	1.18
6	1.16±0.16	1.16	8.75	1.09

2.3. Biocatalytic assay

The reduced state of nicotinamide adenine dinucleotide (NADH) is a control marker of the energy production chain in mitochondria. Studies show that NADH can transfer hydrogen to transition metal complexes and promote the production of reactive oxygen species (ROS, $^1O_2$), which manifests as an antitumor mechanism of oxidation [41, 42]. The interaction between target complexes and NADH was determined by the UV-vis spectrum. As shown in Figures 5a and S9, the maximum absorbance of NAD^+ (oxidation state of NADH after hydrogen loss catalyzed by

target complexes) and NADH can be determined at 259 and 339 nm; meanwhile, a significant increase and decrease occur at 259 nm and 339 nm with the increase in target complexes, which confirms the catalytic characteristics of these complexes with the change of NADH/NAD^+. Additionally, these changes can be effectively expressed by the turnover numbers (TONs, Figure 5b); the values of TONs for complexes **1**, **3**, and **5** (η^5-C_5Me_5) are significantly larger than those of phenyl-modified complexes **2**, **4**, and **6** (η^5-$C_5Me_4C_6H_5$), which is consistent with the results of the cytotoxicity test: the larger the TONs, the better the antitumor activity.

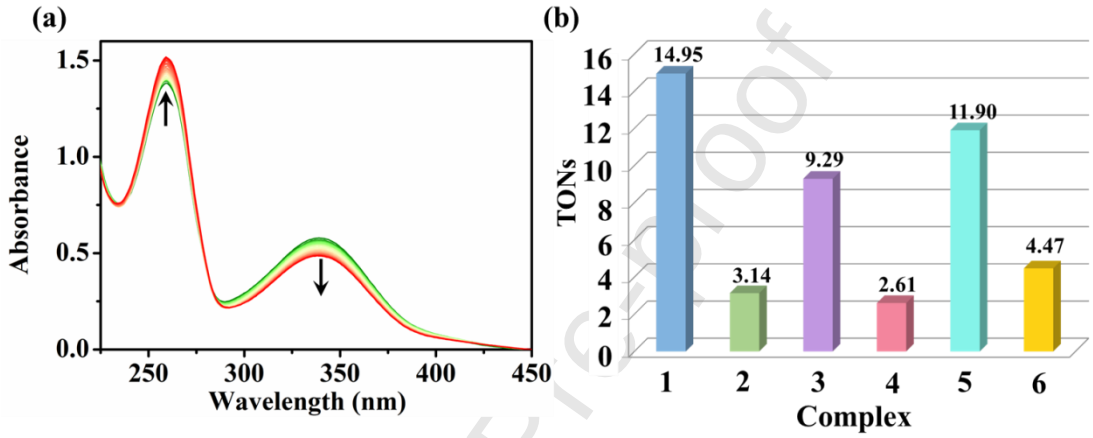

Figure 5. (a) UV-vis spectra of NADH (100.0 μM) with complex **1** (1.0 μM) in 20% MeOH/80% H_2O (v/v) at 298 K for 8 h. The arrows show the changes in the absorbance spectra over time. (b) TONs of target complexes.

The levels of ROS in A549 cells, generated by the catalysis of these Ir^{III} complexes after 24 h, were identified by flow cytometry [43]. As shown in Figure S10, the levels of ROS are nearly 1.16 and 1.08 times that of the negative control for complexes **1** and **2** at the concentration of 0.50 ×IC_{50}, respectively. Compared with complex **2**, the higher ROS levels induced by complex **1** are consistent with the conclusion that complex **1** possesses better antitumor activity. However, the minor TONs and ROS levels also confirmed the limited biocatalysis performance of these compounds.

2.4. Apoptosis assay

To determine whether these Ir^{III} complexes could induce apoptosis, A549 cells were treated with complexes **1** and **2** at the concentrations of 0.5 × IC_{50}, 1.0× IC_{50}, 2.0× IC_{50} and 3.0× IC_{50} for 24 h and then analyzed by flow cytometry [44]. As shown in Figure 6, complexes **1** and **2** can induce apoptosis in a dose-dependent manner and chiefly affect late apoptosis. At the maximal incubated

concentration (3.0 × IC_{50}), the proportions of late apoptosis caused by complexes **1** and **2** were 65.85% and 66.71%, respectively (Tables S4 and S5). However, ~93% cells survived in the control group under the same conditions. This conclusion further confirmed that target Ir^{III} complexes can induce the functional decline of tumor cells and lead to apoptosis. Additionally, Ir^{III} complexes can exert their antitumor effects and induce functional decline by disrupting the cell cycle [45]. As shown (Figure S11, Tables S6 and S7), complexes **1** and **2** mainly lead to 63.89% and 60.15% cell arrest in the G_0/G_1 phase, respectively, compared with the negative control, which increased by 7.87% and 3.29%. The results indicate that these Ir^{III} complexes may restrain the proliferation of A549 cells by cell cycle arrest and, eventually, induce apoptosis.

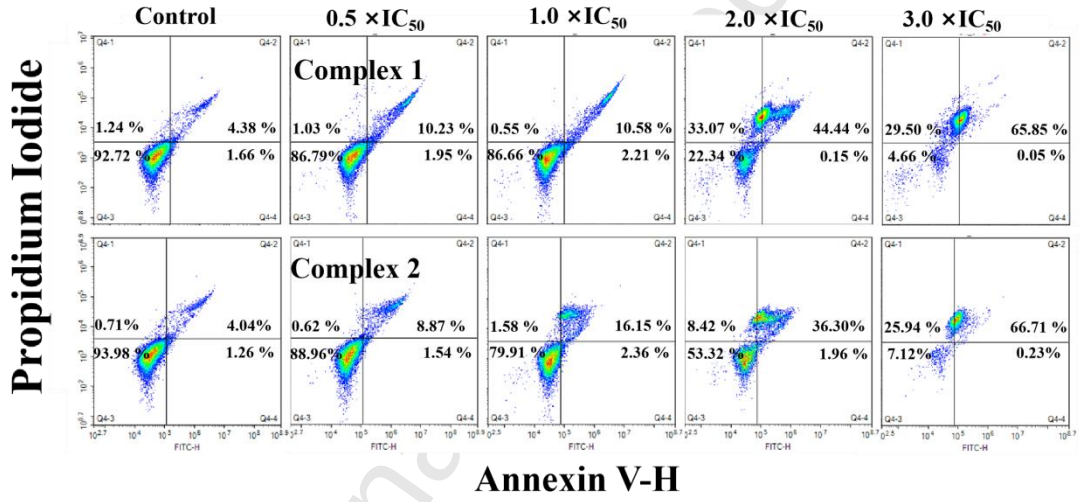

Figure 6. Apoptosis analysis of A549 cells after exposure to complexes **1** and **2** for 24 h at 310 K and determined by flow cytometry using Annexin VFITC/PI staining.

Mitochondria play an irreplaceable role in apoptosis due to their ability to provide biological energy to cells. The decrease of the mitochondrial membrane potential (*MMP*) is a key indicator of cell apoptosis [46, 47]. The effects of complexes **1** and **2** on *MMP* were assessed by JC-1 (5,5′,6,6′-tetrachloro-1,1′,3,3′-tetraethylbenzimidazolylcarbocyanine iodide), an ideal fluorescent probe for detecting *MMP* with red and green fluorescence representing a high and low mitochondrial membrane potential, respectively. As shown in Figure 7, the green fluorescence increased, while the red fluorescence decreased with the addition of complexes **1** and **2**. The percentages of cells with mitochondrial membrane depolarization increased by 62.40% and 62.28% for complexes **1** and **2**, respectively, with concentrations changing from 0.5 × IC_{50} to 2.0 × IC_{50}

(Tables S8 and S9). The increase in the JC-1 green/red fluorescence intensity ratio further confirmed that these Ir^{III} complexes can induce a change in *MMP*, leading to apoptosis.

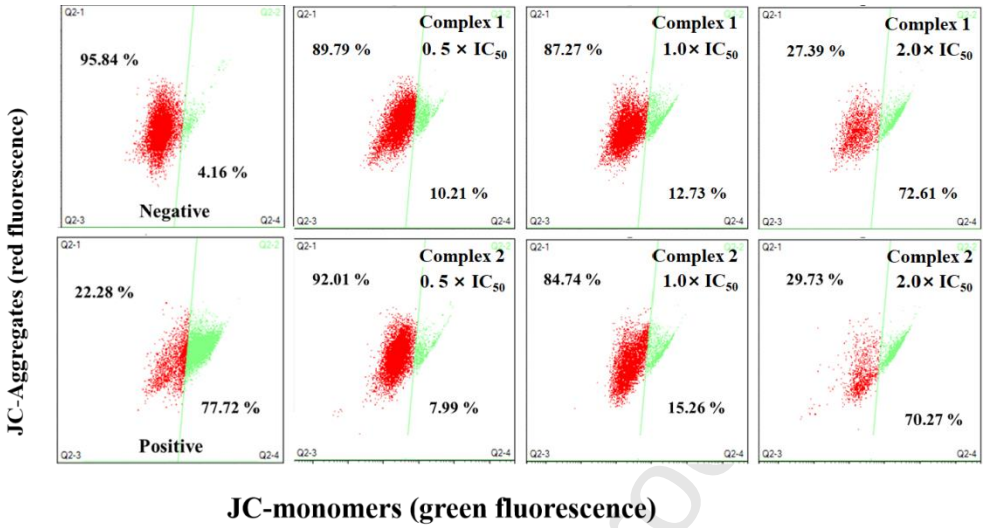

Figure 7. The loss of MMP induced by complexes **1** and **2** at the concentrations of 0.5 × IC_{50}, 1.0 × IC_{50} and 2.0 × IC_{50} using JC-1 staining. The red aggregates and green monomers are gated.

2.5. Cellular uptake mechanism and cellular localization

Favorable cellular uptake mechanism is beneficial to improve the antitumor activity of drugs [48]. The cellular uptake mechanism of complexes **1** and **2** in labeled A549 cells was assessed by laser confocal microscopy. Cellular uptake mechanisms are mainly divided into two types: energy-dependent mechanisms (including active transport and endocytosis) and non-energy-dependent mechanisms (including passive transport and free diffusion) [49]. In this study, A549 cancer cells were incubated with complexes **1** and **2** (10 μM) at 310 K and 277 K and then treated with chlorocyanochlorophenyl (CCCP, metabolic inhibitor, 50 μM) and chloroquine (endocytosis modulator, 50 μM) to ascertain the cell uptake mechanism. Compared with control treatment, there were no significant changes (Figure S12), which indicated that these complexes enter tumor cells, followed by a non-energy-dependent pathway [50].

Due to the favorable targeted luminescence properties of these complexes, laser confocal microscopy was also utilized to determine the co-localization of complexes **1** and **2**. In this study, Lysol Tracker Deep Red (LTDR) and Mito Tracker Deep Red (MTDR) were used as the lysosome and mitochondria fluorescent probes, respectively [51, 52]. As shown in Figure 8, complexes **1** and **2** effectively accumulated in lysosomes with Pearson Colocalization Coefficient (PCC) values

of 0.81 and 0.70, respectively, after incubation for 1 h; however, the values for mitochondria were almost negligible (-0.03 and -0.13, respectively). These results indicate that the introduction of a weakly basic PhCz/TPA unit at the end of C^N chelating ligands (containing electron-rich nitrogen atoms) is beneficial for targeting acidic lysosomes (pH = 4.5-5.5) for these complexes. Interestingly, these complexes do not cause abnormal cell death immediately, which makes it easy to track the changes in cells in real time.

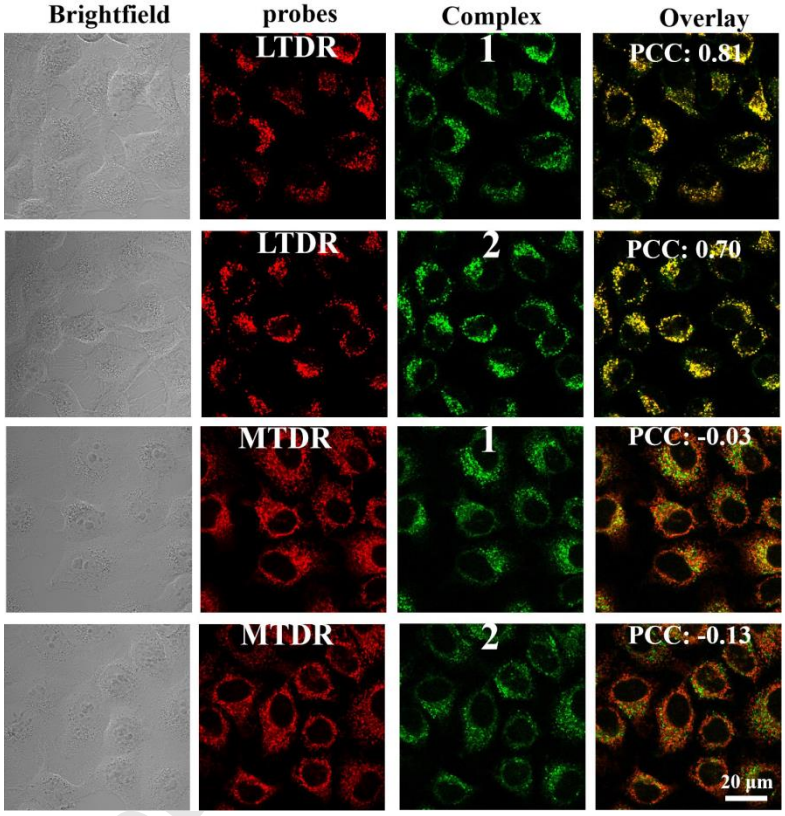

Figure 8. The intercellular localization of complexes **1** and **2** was determined by confocal microscopy after 1 h of incubation. Complexes were excited at 488 nm and collected at 520-580 nm. LTDR was excited at 594 nm and collected at 600-660 nm. MTDR was excited at 543 nm and collected at 660-720 nm.

Lysosomal damage, a process known as lysosomal membrane permeabilization, can lead to the release of cathepsins and other hydrolases from the lysosomal lumen to the cytosol, thus inducing apoptosis [53]. In general, acridine orange (AO) is usually used to determine the integrity of lysosomes [54-56]. Green fluorescence and red fluorescence represent the binding of AO to RNA in the nucleus or cytoplasm and aggregation in the lysosome, respectively. As shown in Figures 9 and S13, lysosomes showed obvious red fluorescence after A549 cells were treated with

only AO (5.0 μM), which indicates the integrity of lysosomes. However, red fluorescence was quickly quenched after exposure to complexes **1** and **2** at concentrations ranging from 1.0 × IC_{50} to 3.0 × IC_{50}, which is the result of increased lysosomal damage. This result is mainly attributable to the introduction of a PhCz/TPA unit, which increased the total alkalinity of target complexes, leading to the accumulation and further damage to the integrity of acidic lysosomes while also explaining the change of *MMP*. This result indicates that target complexes can induce apoptosis by exerting lysosomal damage.

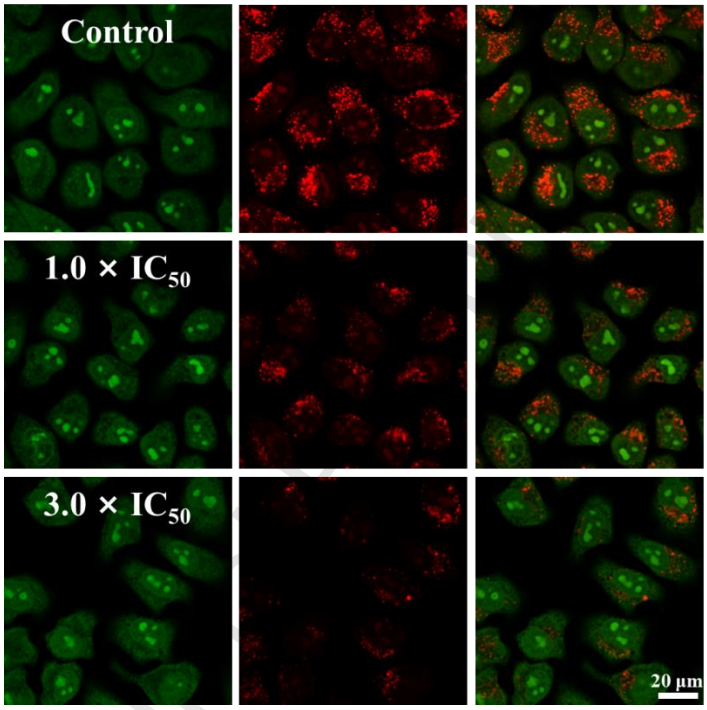

Figure 9. Lysosomal damage in A549 cells caused by complex **1** with AO (5.0 μM) staining.

3. Conclusion

Six PhCz/TPA-appended half-sandwich Ir^{III} phenylpyridine complexes were prepared and characterized. The introduction of the PhCz/TPA unit effectively increased the antitumor activity of these complexes against A549 and HeLa tumor cells, the best of which had activity nearly eight times that of clinical cisplatin and effectively blocked the migration of cancer cells. These complexes can effectively bind to protein, undergo transport through serum proteins, and catalyze the change of NADH to NAD^+, leading to the increased ROS levels in cells. Additionally, flow cytometry and laser confocal microscopy confirmed that these complexes possessed a non-energy-dependent cellular uptake mechanism, effectively accumulated in lysosomes and

damaged the integrity of acidic lysosomes, disrupted the cell cycle, induced a change in the mitochondrial membrane potential, and eventually, induced apoptosis. Above all, PhCz/TPA-appended half-sandwich Ir^{III} phenylpyridine complexes are potential antitumor agents with dual functions: metastasis inhibition and lysosomal damage.

4. Experimental

4.1. General Information

$IrCl_3 \cdot 3H_2O$, 1,2,3,4,5-pentamethyl-cyclopentadiene (95%), *n*-butyl lithium (1.6 M in hexane), 2,3,4,5-tetramethyl-2-cyclopentenone (95%), 2-(4-bromophenyl)pyridine, carbazole, Palladium tetraphenylphosphine, triisopropyl borate, sodium acetate, *N*-bromosuccinimide, triphenylamine, *N,N′*-di(4-methoxyphenyl)phenylamine, 1-bromo-4-iodobenzene were purchased from Ruiya Biotechnology Co., Ltd. 4-bromotriphenylamine, 4-bromo-*N,N′*-di(4-methoxyphenyl)phenylamine, *N*-(4-bromophenyl)carbazole (**M1**) were synthesized according to the literature [57]. 2-pyridyl phenylboronic (**M2**) was synthesized through 2-(4-bromophenyl)pyridine and triisopropyl borate according to the literature [58]. Fetal bovine serum, Nicotinamide adenine dinucleotide, penicillin/streptomycin mixture, trypsin/EDTA, and phosphate-buffered saline (PBS) were purchased from Sangon Biotech. A549 (lung cancer) and HeLa (human cervical cancer) cells were obtained from Shanghai Institute of Biochemistry and Cell Biology (SIBCB). Dimers **1** and **2,** complexes **7** and **8** were synthesized according to the methods of literatures [12] (Scheme S1), the data were shown in supporting information.

NMR spectra were obtained on Bruker DPX 500 spectrometers instrument. Mass spectrum (ESI-MS) was measured on a LCQ Advantage MAX mass spectrometer. Elemental analysis was performed on a VarioMICRO CHNOS elemental analyzer. UV-vis spectroscopy was performed on a PERSEE TU-1901 UV spectrometer. Fluorescence spectra were collected by a Hitachi F-4600 fluorescence spectrophotometer, with a 400 V voltage and 5 nm slit width for both excitation and emission. Induction of apoptosis, cell cycle and mitochondrial membrane potential (MMP) determination were carried out by an ACEA Novocyte2040R flow cytometry. Viability assay (MTT) was measured using a Perlong DNM-9606 microplate reader at an absorbance of 570 nm. Cell uptake and cellular localization were carried out on a Carl Zeiss AG */LSM/880NLO two photon laser Scanning microscope.

The spectrograms of target complexes, the methods of biological performance testing are all shown in Supporting Information.

4.2. Synthesis

*Synthesis of chelating ligands (**L1-L3**)*

C^N chelating ligands were obtained by the classical Suzuki reaction (Scheme 1); the general process is listed as follows: The corresponding brominated PhCz/TPA (4.0 mmol), 4-phenylpyridine-2-boronic acid (4.8 mmol, 0.96 g), palladium tetraphenylphosphine (0.08 mmol, 0.14 g), anhydrous potassium carbonate (8.0 mmol, 1.11 g), 60 mL of toluene and 12 mL of deionized water were added to a 100 mL flask under N_2 and stirred at 383 K for 12 h. The product was extracted with dichloromethane (30 mL×3) and distilled under reduced pressure. Then, the product was purified by chromatography on a silica gel column (petroleum ether: ethyl acetate =15:1 as eluent), and the pure target chelating ligands were obtained. The ^{1}H NMR spectrum, ^{13}C NMR spectrum and ESI-MS of **L1-L3** are presented in Figures S14, S16 and S18. The data were as follows:

L1. Yield: 1.35g (86%). ^{1}H NMR (500 MHz, $CDCl_3$) δ 8.75 (d, *J* = 4.6 Hz, 1H), 8.17 (t, *J* = 7.0 Hz, 4H), 7.90 (d, *J* = 8.3 Hz, 2H), 7.82 (t, *J* = 7.2 Hz, 4H), 7.67 (d, *J* = 8.2 Hz, 2H), 7.50 (d, *J* = 8.2 Hz, 2H), 7.44 (t, *J* = 7.6 Hz, 2H), 7.31 (dd, *J* = 15.6, 8.3 Hz, 3H). ^{13}C NMR (126 MHz, $CDCl_3$) δ 156.89, 149.79, 140.86, 140.75, 139.63, 138.62, 137.14, 136.90, 128.49, 127.52, 127.48, 127.40, 126.03, 123.49, 122.29, 120.54, 120.38, 120.06, 109.88. ESI-MS (*m/z*): calcd for $C_{29}H_{20}N_2$, 396.2; Found 397.2 $[M+H]^+$.

L2. Yield: 1.29g (81%). ^{1}H NMR (500 MHz, $CDCl_3$) δ 8.72 (d, *J* = 4.8 Hz, 1H), 8.07 (d, *J* = 8.4 Hz, 2H), 7.78 (d, *J* = 4.0 Hz, 2H), 7.70 (d, *J* = 8.4 Hz, 2H), 7.54 (d, *J* = 8.7 Hz, 2H), 7.28 (dd, *J* = 8.4, 7.6 Hz, 5H), 7.17 – 7.11 (m, 6H), 7.04 (t, *J* = 7.3 Hz, 2H). ^{13}C NMR (126 MHz, $CDCl_3$) δ 157.07, 149.69, 147.64, 147.48, 141.19, 137.69, 136.81, 134.32, 129.33, 127.74, 127.30, 126.91, 124.53, 123.82, 123.05, 122.05, 120.40. ESI-MS (*m/z*): calcd for $C_{29}H_{22}N_2$, 398.2; Found 398.2 [M].

L3. Yield: 1.45g (83%). ^{1}H NMR (500 MHz, $CDCl_3$) δ 8.76 (d, *J* = 4.3 Hz, 1H), 8.09 (d, *J* = 8.1 Hz, 2H), 7.85 (s, 2H), 7.70 (d, *J* = 8.2 Hz, 2H), 7.48 (d, *J* = 8.6 Hz, 2H), 7.34 (s, 1H), 7.10 (d, *J* = 8.8 Hz, 4H), 7.00 (d, *J* = 8.6 Hz, 2H), 6.85 (d, *J* = 8.9 Hz, 4H), 3.81 (s, 6H). ^{13}C NMR (126 MHz, $CDCl_3$) δ 156.03, 149.16, 142.01, 141.08, 140.75, 139.66, 138.38, 129.33, 127.52, 126.83, 126.76,

124.58, 123.89, 123.10, 121.24, 120.51, 114.76, 55.52. ESI-MS (*m/z*): calcd for $C_{31}H_{26}O_2N_2$, 458.2; Found 459.2 $[M+H]^+$.

Synthesis of [(η^5-Cp)Ir(C^N)Cl] (Complexes **1-6**)*

[(η^5-Cp^x)$IrCl_2$]$_2$ (dimer, 0.05 mmol, 1 *equiv,*), chelating ligand **L** (0.1 mmol, 2 *equiv*) and sodium acetate (0.6 mmol, 10 *equiv*) in methanol (40 mL) were stirred at ambient temperature overnight. The solvent was removed under reduced pressure, and 20 mL of dichloromethane was added, after which the precipitate (sodium acetate) was removed by filtration. Most of the solvent was concentrated to 2.0 mL under vacuum and kept at 253 K for 12 h, filtered and washed with cold methanol and diethyl ether. The ^{1}H NMR, ESI-MS and ^{13}C NMR spectrum of complexes **1-6** are presented in Figures S15, S17 and S19. The data were as follows:

[(η^5-C_5Me_5)Ir(L1)Cl] (1). Yield: 77.3 mg (85%). ^{1}H NMR (500 MHz, $CDCl_3$) δ 8.74 (d, *J* = 5.2 Hz, 1H), 8.19 – 8.13 (m, 3H), 7.93 (d, *J* = 8.4 Hz, 2H), 7.88 (d, *J* = 8.1 Hz, 1H), 7.80 (d, *J* = 8.0 Hz, 1H), 7.72 – 7.68 (m, 1H), 7.65 (d, *J* = 8.4 Hz, 2H), 7.52 (d, *J* = 8.2 Hz, 2H), 7.44 (t, *J* = 7.7 Hz, 2H), 7.39 (dd, *J* = 8.0, 1.7 Hz, 1H), 7.31 (t, *J* = 7.4 Hz, 2H), 7.12 (dd, *J* = 9.5, 3.5 Hz, 1H), 1.75 (s, 15H). ^{13}C NMR (126 MHz, $CDCl_3$) δ 166.90, 163.86, 151.45, 143.91, 142.00, 141.13, 140.96, 137.08, 136.62, 134.34, 128.68, 127.22, 125.97, 124.21, 123.41, 122.41, 121.44, 120.30, 119.91, 119.10, 109.98, 88.68, 9.08. Elemental Analysis: Found: C, 61.81; H, 4.60; N, 3.63%, calcd for C, 61.77; H, 4.52; N, 3.69%. ESI-MS (*m/z*): calcd for $C_{39}H_{34}N_2Ir$: 723.2, Found: 723.3 $[M-Cl]^+$.

[(η^5-$C_5Me_4C_6H_5$)Ir(L1)Cl] (2). Yield: 80.7 mg (82%). ^{1}H NMR (500 MHz, $CDCl_3$) δ 8.56 (d, *J* = 5.2 Hz, 1H), 8.17 (d, *J* = 7.7 Hz, 2H), 7.98 (d, *J* = 1.6 Hz, 1H), 7.87 (d, *J* = 8.0 Hz, 1H), 7.80 (d, *J* = 8.1 Hz, 1H), 7.76 (d, *J* = 8.4 Hz, 2H), 7.67 (td, *J* = 8.1, 1.4 Hz, 1H), 7.57 (d, *J* = 8.4 Hz, 2H), 7.52 – 7.38 (m, 9H), 7.36 (t, *J* = 7.3 Hz, 1H), 7.33 – 7.29 (m, 2H), 7.02 – 6.96 (m, 1H), 1.90 (s, 3H), 1.79 (d, *J* = 3.5 Hz, 6H), 1.67 (s, 3H). ^{13}C NMR (126 MHz, $CDCl_3$) δ 166.89, 162.89, 151.59, 143.79, 141.62, 140.92, 140.63, 137.17, 136.58, 133.92, 132.37, 131.02, 128.74, 128.45, 127.33, 127.09, 125.96, 124.30, 123.40, 122.43, 121.35, 120.31, 119.91, 119.11, 109.96, 98.33, 97.95, 86.26, 85.19, 83.83, 14.14, 10.36, 9.92, 8.97. Elemental Analysis: Found: C, 64.51; H, 4.50; N, 3.40%, calcd for C, 64.41; H, 4.42; N, 3.41%. ESI-MS (*m/z*): calcd for $C_{44}H_{36}N_2Ir$: 785.3, Found: 785.3 $[M-Cl]^+$.

[(η^5-C_5Me_5)Ir(L2)Cl] (3). Yield: 73.9 mg (81%). ^{1}H NMR (500 MHz, $CDCl_3$) δ 8.70 (d, *J* = 5.6 Hz, 1H), 8.04 (d, *J* = 1.7 Hz, 1H), 7.82 (d, *J* = 8.1 Hz, 1H), 7.71 (d, *J* = 8.1 Hz, 1H), 7.67 – 7.64

(m, 1H), 7.60 (d, *J* = 8.6 Hz, 2H), 7.29 (d, *J* = 8.2 Hz, 5H), 7.15 (dd, *J* = 8.1, 4.5 Hz, 6H), 7.06 (ddd, *J* = 18.4, 10.9, 4.3 Hz, 3H), 1.71 (s, 15H). ^{13}C NMR (126 MHz, CDCl3) δ 167.03, 163.64, 151.36, 147.80, 147.02, 143.09, 142.37, 136.98, 135.93, 133.81, 129.28, 127.98, 124.43, 124.12, 123.91, 122.84, 122.11, 120.93, 118.92, 88.57, 9.04. Elemental Analysis: Found: C, 61.71; H, 4.90; N, 3.63%, calcd for C, 61.60; H, 4.77; N, 3.68%. ESI-MS (*m/z*): calcd for $C_{39}H_{36}N_2Ir$: 725.3, Found: 725.3 $[M\text{-}Cl]^+$.

[(η^5-$C_5Me_4C_6H_5$)Ir(L2)Cl] (4). Yield: 81.9 mg (83%). ^{1}H NMR (500 MHz, $CDCl_3$) δ 8.49 (d, *J* = 5.6 Hz, 1H), 7.89 (d, *J* = 1.6 Hz, 1H), 7.81 (d, *J* = 8.0 Hz, 1H), 7.72 (d, *J* = 8.1 Hz, 1H), 7.64 – 7.60 (m, 1H), 7.45 (t, *J* = 7.9 Hz, 4H), 7.39 – 7.32 (m, 3H), 7.28 (d, *J* = 8.2 Hz, 4H), 7.14 (d, *J* = 7.6 Hz, 5H), 7.08 (d, *J* = 8.6 Hz, 2H), 7.03 (t, *J* = 7.3 Hz, 2H), 6.95 – 6.91 (m, 1H), 1.83 (s, 3H), 1.77 (s, 6H), 1.61 (s, 3H). ^{13}C NMR (126 MHz, $CDCl_3$) δ 167.01, 162.64, 151.51, 147.75, 142.14, 137.00, 133.34, 132.34, 131.17, 130.93, 129.89, 129.23, 128.67, 127.80, 127.28, 126.42, 124.37, 124.19, 123.81, 122.79, 122.08, 120.92, 118.87, 96.68, 94.72, 89.67, 87.80, 85.92, 10.23, 9.88, 8.96, 8.90. Elemental Analysis: Found: C, 64.29; H, 4.80; N, 3.43%, calcd for C, 64.26; H, 4.66; N, 3.41%. ESI-MS (*m/z*): calcd for $C_{44}H_{38}N_2Ir$: 787.3, Found: 787.4 $[M\text{-}Cl]^+$.

[(η^5-C_5Me_5)Ir(L3)Cl] (5). Yield: 80.7 mg (82%). ^{1}H NMR (500 MHz, $CDCl_3$) δ 8.69 (d, *J* = 5.7 Hz, 1H), 8.02 (d, *J* = 1.6 Hz, 1H), 7.80 (d, *J* = 8.1 Hz, 1H), 7.69 (d, *J* = 8.1 Hz, 1H), 7.66 – 7.62 (m, 1H), 7.54 (d, *J* = 8.6 Hz, 2H), 7.24 (d, *J* = 1.7 Hz, 1H), 7.11 (d, *J* = 8.8 Hz, 4H), 7.07 – 7.04 (m, 1H), 7.00 (d, *J* = 8.5 Hz, 2H), 6.85 (d, *J* = 8.9 Hz, 4H), 3.81 (s, 6H), 1.70 (s, 15H). ^{13}C NMR (126 MHz, $CDCl_3$) δ 167.10, 163.58, 155.83, 151.32, 147.98, 142.76, 142.56, 141.04, 136.91, 133.84, 133.60, 127.74, 126.61, 124.08, 121.98, 120.76, 118.84, 115.82, 114.71, 88.53, 55.53, 9.02. Elemental Analysis: Found: C, 60.21; H, 5.10; N, 3.43%, calcd for C, 60.02; H, 4.91; N, 3.41%. ESI-MS (*m/z*): calcd for $C_{41}H_{40}N_2O_2Ir$: 785.3, Found: 785.4 $[M\text{-}Cl]^+$.

[(η^5-$C_5Me_4C_6H_5$)Ir(L3)Cl] (6). Yield: 88.9 mg (84%). ^{1}H NMR (500 MHz, $CDCl_3$) δ 8.48 (d, *J* = 5.3 Hz, 1H), 7.88 (s, 1H), 7.80 (d, *J* = 8.1 Hz, 1H), 7.70 (d, *J* = 8.1 Hz, 1H), 7.60 (dd, *J* = 11.2, 4.3 Hz, 1H), 7.46 (d, *J* = 7.0 Hz, 2H), 7.42 – 7.28 (m, 6H), 7.09 (d, *J* = 7.3 Hz, 4H), 6.92 (dd, *J* = 15.6, 8.5 Hz, 3H), 6.85 (d, *J* = 8.6 Hz, 4H), 3.81 (s, 6H), 1.82 (s, 3H), 1.77 (d, *J* = 0.8 Hz, 6H), 1.59 (s, 3H). ^{13}C NMR (126 MHz, $CDCl_3$) δ 166.04, 162.67, 150.45, 146.55, 146.36, 146.20, 141.59, 139.99, 135.94, 132.09, 131.33, 129.90, 128.59, 127.64, 126.54, 126.24, 125.52, 123.15, 120.94, 119.75, 119.64, 117.78, 113.64, 98.50, 95.34, 85.09, 84.68, 82.10, 54.49, 13.10, 9.17, 8.85, 7.87.

Elemental Analysis: Found: C, 62.71; H, 5.10; N, 3.23%, calcd for C, 62.61; H, 4.80; N, 3.17%. ESI-MS (*m/z*): calcd for $C_{46}H_{42}N_2O_2Ir$: 847.3, Found: 847.4 $[M\text{-}Cl]^+$.

Abbreviations

LMP: Lysosomal Membrane Permeabilization

Cp: pentamethylcyclopentadienyl

TPA: Triphenylamine

PhCz: *N*-phenylcarbazole

A549: human lung cancer cells

Hela: human cervical cancer cells

BEAS-2B: human lung epithelial cells

MTT: 3-(4,5-dimethylthiazol-2-yl)-2,5-diphenyl tetrazolium bromide

NPA: Natural Population Analysis

WCR: Wounds Closure Ratio

BSA: Bovine Serum Albumin

NADH: reduced state of Nicotinamide Adenine Dinucleotide

ROS: Reactive Oxygen Species

MMP: mitochondrial membrane potential

PCC: Pearson Colocalization Coefficient

Declaration of Competing Interest

The authors declare no competing financial interest.

Acknowledgments

We thank the University Research Development Program of Shandong Province (J18KA082), the Student's Platform for Innovation and Entrepreneurship Training Program (2018A043), the National Natural Science Foundation of China (Grant No. 21671118 and 21703118), the Taishan Scholars Program and the High Performance Computing Center of Qufu Normal University for support.

References

[1] U. Repnik, B. Turk, Mitochondrion 10 (2010) 662-669.

[2] M.E. Guicciardi, M. Leist, G.J Gores, Oncogene 23 (2004) 2881-2890.

[3] J.P. Luzio, P.R. Pryor, N.A. Bright, Nat. Rev. Mol. Cell Biol. 8 (2007) 622-632.

[4] A. Serrano-Puebla, P. Boya, Ann. N. Y. Acad. Sci. 1371 (2016) 30-44.

[5] P. Saftig, J. Klumperman, Nat. Rev. Mol. Cell Biol. 10 (2009) 623-635.

[6] J.J. Li, X.C. Liu, H.F. Zhang, X.X. Ge, Y.H. Tang, Z.S. Xu, L.J. Tian, X.-A. Yuan, X.D. Mao, Z. Liu, Inorg. Chem. 58 (2019) 1710-1718.

[7] B. Sun, J. Liu, Y. Gao, H.B. Zheng, L. Li, Q.W. Hu, H.Q. Yuan, H.X. Lou, Eur. J. Med. Chem. 136 (2017) 603-618.

[8] B. Rosenberg, L. Vancamp, J.E. Trosko, V.H. Mansour, Nature 222 (1969) 385-386.

[9] Y. Shi, S.A. Liu, D.J. Kerwood, J. Goodisman, J.C. Dabrowiak, J. Inorg. Biochem. 107 (2012) 6–14.

[10] S.J. Lucas, R.M. Lord, R.L. Wilson, R.M. Phillips, V. Sridharan, P.C. McGowan, Dalton Trans. 41 (2012) 13800–13802.

[11] J. Ruiz, C. Vicente, C. de Haro, D. Bautista, Inorg. Chem. 52 (2013**)** 974−982.

[12] Z. Liu, P.J. Sadler, Acc. Chem. Res. 47 (2014) 1174-1185.

[13] K.K.W. Lo, K.Y. Zhang, RSC Adv. 2 (2012) 12069–12083.

[14] X.D. He, X.C. Liu, Y.H. Tang, J.Y. Du, M. Tian, Z.S. Xu, X.Y. Liu, Z. Liu, Dyes Pigments 160 (2019) 217–226.

[15] K.Q. Qiu, J.Q. Wang, C.L. Song, L.L. Wang, H.Y. Zhu, H.Y. Huang, J.J. Huang, H. Wang, L.N. Ji, H. Chao, ACS Appl. Mater. Interfaces 8 (2016) 12702-12710.

[16] F.X. Wang, M.H. Chen, Y.N. Lin, H. Zhang, C.P. Tan, L.N. Ji, Z.W. Mao, ACS Appl. Mater. Interfaces 9 (2017) 42471-42481.

[17] Y.L. Han, X.C. Liu, Z.Z. Tian, X.X. Ge, J.J. Li, M. Gao, Y.R. Li, Y. Liu, Z. Liu, Chem. Asian J. 13 (2018) 3697-3705.

[18] W.L. Ma, Z.Z. Tian, S.M. Zhang, X.D. He, J.J. Li, X.R. Xia, X.B. Chen, Z. Liu, Inorg. Chem. Front. 5 (2018) 2587–2597.

[19] L. He, Y. Li, C.P. Tan, R.R. Ye, M.H. Chen, J.J. Cao, L.N. Ji, Z.-W. Mao, Chem. Sci. 6 (2015) 5409-5418.

[20] X.C. Liu, J.F. Liang, J. You, L. Ying, Y. Xiao, S.R. Wang, X.G. Li, Dyes Pigments 131 (2016)

41-48.

[21] X.C. Liu, F. Zhang, Z. Liu, Y. Xiao, S.R. Wang, X.G. Li, J. Mater. Chem. C 5 (2017) 11429-11435.

[22] X.M. Zhao, F. Zhang, C.Y. Yi, D.Q. Bi, X.D. Bi, P. Wei, J.S. Luo, X.C. Liu, S.R. Wang, X.G. Li, S.M. Zakeeruddin, M. Grätzel, J. Mater. Chem. A 4 (2016) 16330-16334.

[23] F. Zhang, X.M. Zhao, C.Y. Yi, D.Q. Bi, X.D. Bi, P. Wei, X.C. Liu, S.R. Wang , X.G. Li, S.M. Zakeeruddin, M.Grätzel, Nano Energy 41 (2017) 469-475.

[24] Y. Shirota, H. Kageyama, Chem. Rev. 107 (2007) 953-1010.

[25] T.P. Bender, J.F. Graham, J.M. Duff, Chem. Mater. 13 (2001) 4105-4111.

[26] K.M. Omer, S.Y. Ku, J.Z. Cheng, S.H. Chou, K.T. Wong, A.J. Bard, J. Am. Chem. Soc. 133 (2011) 5492–5499.

[27] H.B. Xiao, Y.Z. Zhang, S.Z. Li, W. Zhang, Z.Y. Han, J.J. Tan, S.Y. Zhang, J.Y. Du, Sens. Actuators, B 236 (2016) 233–240.

[28] F.F. Xue, Y. Lu, Z.G. Zhou, M. Shi, Y.P. Yan, H. Yang, S.P. Yang, Organometallics 34 (2015) 73-77.

[29] N.E. Leadbeater, M. Marco, Org. Lett. 4 (2002) 2973-2976.

[30] Z. Liu, I. Romero-Canelon, A. Habtemariam, G.J. Clarkson, P.J. Sadler, Organometallics 33 (2014) 5324-5333.

[31] M. J. Frisch, G. W. Trucks, H. B. Schlegel, G. E. Scuseria, M. A. Robb, J. R. Cheeseman, *et al.* Gaussian 09, revision D.01; Gaussian, Inc.: Wallingford, CT, 2013.

[32] X.A. Yuan, W.W. Zhang, L.H. Xie, J. Ma, W. Huang, W.J. Liu, J. Phys. Chem. B 119 (2015) 10316-10333.

[33] Q.J. He, J.L. Shi, Adv. Mater. 26 (2014) 391-411.

[34] O. Dömötör, C.G. Hartinger, A.K. Bytzek, T. Kiss, B.K. Keppler, E.A. Enyedy, J. Biol. Inorg. Chem. 18 (2013) 9-17.

[35] M.E. Pacheco, L. Bruzzone, J. Lumin. 137 (2013) 138-142.

[36] D.S. Raja, G. Paramaguru, N. S. P. Bhuvanesh, J.H. Reibenspies, R. Renganathan, K. Natarajan, Dalton Trans. 40 (2011) 4548-4559.

[37] Y.Z. Zhang, B. Zhou, Y.X. Liu, C.X. Zhou, X.L. Ding, Y. Liu, J. Fluoresc. 18 (2008) 109-118.

[38] M.R. Eftink, C.A.Ghiron, J. phys. Chem. 80 (1976) 486-493.

[39] A. Castiñeiras, N. Fernández-Hermidan, I. García-Santos, L. Gómez-Rodríguez, Dalton Trans. 41 (2012) 3486-3495.

[40] J.H. Tang, F. Luan, X.G. Chen, Biorg. Med. Chem. 14 (2006) 3210-3217.

[41] Z.J. Cheng, J. Lumin. 132 (2012) 2719-2729.

[42] S. Betanzos-Lara, Z. Liu, A. Habtemariam, A.M. Pizarro, B. Qamar, P.J. Sadler, Angew. Chem. Int. Ed. 51 (2012) 3897-3900.

[43] Z. Liu, R.J. Deeth, J.S. Butler, A. Habtemariam, M.E. Newton, P.J.Sadler, Angew. Chem. Int. Ed. 52 (2013) 4194-4197.

[44] I. Romero-Canelon, M. Mos, P.J. Sadler, J. Med. Chem. 58 (2015) 7874-7880.

[45] X. D. He, M. Tian, X.C. Liu, Y.H. Tang, C.F. Shao, P.W. Gong, J.F. Liu, S.M. Zhang, L.H. Guo, Z. Liu, Chem. Asian J. 13 (2018) 1500 – 1509.

[46] V. Novohradsky, L. Zerzankova, J. Stepankova, A. Kisova, H. Kostrhunova, Z. Liu, P.J. Sadler, J. Kasparkova, V. Brabec, Metallomics 6 (2014) 1491-1501.

[47] H. Antonicka, K. Choquet, Z.Y. Lin, A.C. Gingras, C.L. Kleinman, E.A. Shoubridge, Embo. Rep. 18 (2017) 28-38.

[48] C.Qian, J. Wang, C. Song, L. Wang, L. Ji, H. Chao, Metallomics 5 (2013) 844-854.

[49] Y.Y. Jiang, G.H. Liu, X.R. Wang, J.M. Hu, G.Y. Zhang, S.Y. Liu, Macromolecules 48 (2015) 764-774.

[50] C. Jin, J. Liu, Y. Chen, G. Li, R. Guan, P. Zhang, L. Ji, H. Chao, Dalton Trans. 44 (2015) 7538–7547.

[51] C.Y. Li, M.X. Yu, Y. Sun, Y.Q. Wu, C.H. Huang, F.Y. Li, J. Am. Chem. Soc. 133 (2011**)** 11231-11239.

[52] S. Daum, V. Reshetnikov, M. Sisa, T. Dymych, M.D. Lootski, R. Bilyy, E. Bila, C. Janko, C. Alexiou, M. Herrmann, L. Sellner, A. Mokhir, Angew. Chem. Int. Ed. 56 (2017) 15545–15549.

[53] Y. Zheng, L. He, D. Y. Zhang, C. P. Tan, L.-N Ji, Z. W. Mao, Dalton Trans. 46 (2017) 11395–11407.

[54] J. Yang, J.X. Zhao, Q. Cao, L. Hao, D.X. Zhou, Z.J. Gan, L.N. Ji, Z.W. Mao, Acs Appl. Mater Inter. 9 (2017) 13900-13912.

[55] X.X. Ge, S.J. Chen, X.C. Liu, Q.H. Wang, L.J. Gao, C.F. Zhao, L. Zhang, M.S. Shao, X.A. Yuan, L.J. Tian, Z. Liu, Inorg. Chem. 58 (2019) 14175−14184.

[56] H. Xu, K.Yin, W. Huang, Chem. Eur. J. 13 (2007) 10281-10293.

[57] S. Mabrouk, M.M. Zhang, Z.H. Wang, M. Liang, B. Bahrami, Y.G. Wu, J.H. Wu, Q.Q. Qiao, S.F. Yang, J. Mater. Chem. A 6 (2018) 7950–7958.

[58] X.X Ge, X.C. Liu, Z.Z. Tian, S.J. Chen, X.Y. Liu, L.H. Guo, P.W. Gong, B.P. Ling, X.A. Yuan, Z. Liu, Appl Organometal Chem. (2019) 5171.

Graphical Abstract

Dual functions of Iridium(III) 2-phenylpyridine complexes: metastasis inhibition and lysosomal damage

Xicheng Liu[+]*, Shujiao Chen[+], Xingxing Ge, Ying Zhang, Yaoqi Xie, Yingying Hao, Daiqun Wu, Jinmin Zhao, Xiang-Ai Yuan, Laijin Tian, Zhe Liu*

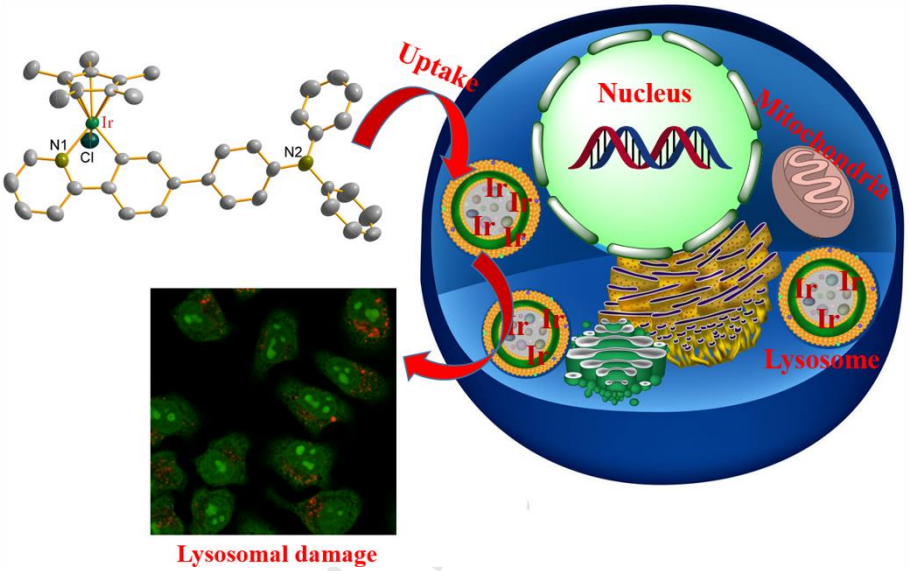

N-phenylcarbazole/triphenylamine-appended half-sandwich iridium(III) 2-phenylpyridine complexes exhibited potential anticancer activity against A549 and HeLa cells. Complexes could enter cells followed by non-energy-dependent cellular uptake mechanism, accumulate in lysosomes, lead to lysosomal damage and eventually induce apoptosis.

Highlights

1. Triphenylamine derivatives-appended iridium complexes exhibit antitumor activity.
2. Complexes inhibit the migration of tumor cells and induce lysosomal damage.
3. Complexes disrupt the cell cycle and induce apoptosis.